PNAS Nexus

PNAS Nexus, 2022, **1**, 1–15
https://doi.org/10.1093/pnasnexus/pgac109
Advance access publication date: 8 July 2022
Research Report

Mechanisms of phase-separation-mediated cGAS activation revealed by dcFCCS

Yirong Yao[a], Wenjuan Wang[b] and Chunlai Chen[a,*]

[a]School of Life Sciences, Beijing Advanced Innovation Center for Structural Biology, Beijing Frontier Research Center of Biological Structure, Tsinghua University, Beijing, 100084, China
[b]School of Life Sciences, Technology Center for Protein Sciences, Tsinghua University, Beijing, 100084, China
*To whom correspondence should be addressed: Email: chunlai@tsinghua.edu.cn
Edited By: Karsten Hiller

Abstract

Cyclic GMP–AMP synthase (cGAS), as a DNA sensor, plays an important role in cGAS–STING pathway, which further induces expression of type I interferon as the innate immune response. Previous studies reported that liquid–liquid phase separation (LLPS) driven by cGAS and long DNA is essential to promote catalytic activity of cGAS to produce a second messenger, cyclic GMP–AMP (cGAMP). However, the molecular mechanism of LLPS promoting cGAS activity is still unclear. Here, we applied dual-color fluorescence cross-correlation spectroscopy (dcFCCS), a highly sensitive and quantitative method, to characterize phase separation driven by cGAS and DNA from miscible individual molecule to micronscale. Thus, we captured nanoscale condensates formed by cGAS at close-to-physiological concentration and quantified their sizes, molecular compositions and binding affinities within condensates. Our results pinpointed that interactions between DNA and cGAS at DNA binding sites A, B, and C and the dimerization of cGAS are the fundamental molecular basis to fully activate cGAS *in vitro*. Due to weak binding constants of these sites, endogenous cGAS cannot form stable interactions at these sites, leading to no activity in the absence of LLPS. Phase separation of cGAS and DNA enriches cGAS and DNA by 2 to 3 orders of magnitude to facilitate these interactions among cGAS and DNA and to promote cGAS activity as an on/off switch. Our discoveries not only shed lights on the molecular mechanisms of phase-separation-mediated cGAS activation, but also guided us to engineer a cGAS fusion, which can be activated by 15 bp short DNA without LLPS.

Significance Statement:

cGAS needs to form high-order oligomerization and liquid–liquid phase separation with long DNA to activate its downstream immune pathway. However, the molecular mechanism of phase-separation-mediated cGAS activation is unclear. Here, with the highly sensitive dcFCCS method, we captured nanoscale condensates formed by cGAS and DNA under close-to-physiological conditions and quantified their sizes, molecular compositions, and binding affinities within condensates. Based on our new findings, we proposed that having DNA binding sites A/B/C and dimer interface bound is the fundamental molecular basis to activate cGAS. Phase separation provides a highly concentrated microenvironment to ensure binding of these weak-interacting sites. Guided by our model, a cGAS fusion is engineered and can be highly activated by short DNA without phase separation.

Introduction

As important parts of the innate immune system, germline-encoded pattern recognition receptors (PRRs) specifically recognize DNA, as a potential marker to indicate infection or cellular damage, to trigger downstream pathways in inflammation, immunity, and pathogen resistance (1–3). A dozen of DNA sensor proteins have been identified as the PRRs in recent years, including the well-known toll-like receptor (TLR9), absent in melanoma (AIM2) and cyclic GMP–AMP synthase (cGAS), which play important roles in different types of cells (4–6). cGAS catalyzes the production of an endogenous second messenger 2′–3′ cyclic GMP–AMP (cGAMP) from substrates ATP and GTP (7, 8). Synthesized cGAMP activates endoplasmic-reticulum-resident membrane adaptor (STING), which eventually induces the production of type I interferon (9–11). The defense against bacteria (*Mycobacterium tuberculosis*), DNA viruses (adenovirus), and retroviruses (HIV-1) through the cGAS–STING pathway have been revealed (12–16). Recent studies reported that SARS-CoV-2 infection induces an immune response through the cGAS–STING pathway, whereas its viral protease can inhibit the cGAS–STING signal pathway (17–19). Furthermore, the cGAS–STING pathway also induces antitumor immunity via sensing tumor-derived cytosolic DNA (20–22). Together, cGAS, as an initial DNA sensor, plays essential roles in the immune signaling pathways.

cGAS activation requires direct binding to double-stranded DNA (dsDNA) to form cGAS–dsDNA complexes, within which the catalytic site of cGAS is structurally rearranged to activate its enzymatic activity to synthesize cGAMP (23–28). Both *in vitro* and *in vivo* studies have shown that interactions between cGAS and DNA result in high-order oligomerization and formation of

Competing Interest: The authors declare no competing interest.
Received: June 7, 2022. **Accepted:** July 2, 2022
© The Author(s) 2022. Published by Oxford University Press on behalf of the National Academy of Sciences. This is an Open Access article distributed under the terms of the Creative Commons Attribution-NonCommercial-NoDerivs licence (https://creativecommons.org/licenses/by-nc-nd/4.0/), which permits non-commercial reproduction and distribution of the work, in any medium, provided the original work is not altered or transformed in any way, and that the work is properly cited. For commercial re-use, please contact journals.permissions@oup.com

liquid–liquid phase separation (LLPS) (29–31). LLPS of biomacromolecules have been reported to be crucial in diverse biological processes, including RNA processing, TLR signaling and B cell receptor (BCR) signaling (32–37). DNA-induced LLPS of cGAS, driven by multivalent interactions between cGAS and DNA, is essential *in vivo* to induce cGAS activation and to trigger the cGAS–STING signaling pathway (30, 38). On the other hand, mutation and truncation of cGAS and short DNA (< 45 bp) attenuate the oligomerization and LLPS of cGAS–DNA, resulting in reduced or even eliminated cGAS activity (29, 30, 39). DNA-induced liquid phase condensation of cGAS has been hypothesized to serve a microreactor to accelerate cGAMP production by increasing local concentrations of proteins and reactants (40). Further studies also demonstrated that cGAS–DNA condensates protect DNA from DNA exonuclease (TREX1) degradation to aid cGAMP production (41). However, the molecular mechanisms regarding how DNA-induced LLPS of cGAS leads to a none-to-all transition in cGAS activity remain unclear, because structures of cGAS–DNA suggest that DNA binding should be sufficient to activate cGAS. In addition, the physiological concentration of cGAS in cell is estimated around 10 nM (30), which is lower than the critical concentration to form micron-scale condensates identified in previous studies (30 to 50 nM). Whether cGAS is able to form nanoscale condensates with cGAMP production activity remains unknown.

Recently, we applied dual-color fluorescence cross-correlation spectroscopy (dcFCCS) to quantitatively examine the dynamic formation of nanoscale condensates driven by LLPS (42). Although dynamic light scattering (DLS) is a commonly used method to quantify radius of freely diffusing particles in solution (43), it requires high concentration (1 to 10 μM), which is far above the physiological concentrations of many biomolecules. The single-molecule sensitivity provided by dcFCCS enabled us to systematically examine formation of cGAS–DNA condensates from miscible individual molecule to micronscale. Thus, for the first time, we revealed that cGAS at its physiological concentration is able to form nanoscale condensates with DNA, beyond the detection limit of the conventional fluorescence microscopy, to fully promote its activity. Besides the size of cGAS–DNA condensates, dcFCCS can quantify additional important unknown properties, including molecular compositions and binding affinities within condensates, which allow us to perform a comprehensive survey to understand how cGAS activity is regulated by phase-separation-induced condensation. Our results revealed that the dimerization of cGAS and interactions between DNA and cGAS at three binding interfaces (sites A, B, and C) are the fundamental molecular basis to activate cGAS. The function of phase separation is to enrich concentrations of cGAS and DNA by 2 to 3 orders of magnitude to permit these interactions, whose binding affinities are low and cannot be permitted under physiological concentrations. Guided by our mechanistic insight, we engineered a fusion cGAS, which can be activated by 15 bp DNA without LLPS.

Results

Quantification of cGAS–DNA condensates at the nanoscale via dcFCCS

We expressed, purified and labeled full-length human cGAS (FL-cGAS) protein with fluorophore Alexa Fluor 488 (AF488) or Cyanine5 (Cy5) (24). Labeling procedure was carefully optimized, so that cGAS was nearly 100% labeled and cGAMP production activity of labeled FL-cGAS was almost the same as the unlabeled one (Figure S1A–D and Tables S1 and S2, Supplementary Material). With a conventional fluorescence microscope, liquid phase condensates formed at the micronscale were captured after mixing AF488-labeled FL-cGAS (AF488-FL-cGAS) and Cy5-labeled DNA (Cy5-DNA) together as previously reported (Figure S1E and F, Supplementary Material).

Next, we applied dcFCCS method to quantify the size and molecular stoichiometry of condensates formed from AF488-FL-cGAS and 99 bp Cy5-DNA (Fig. 1). DNA sequence was based on the one used in previous study and shown in Table S3 (Supplementary Material) (30). When concentrations of AF488-FL-cGAS increased from 0.5 to 200 nM and [AF488-FL-cGAS]/[Cy5-DNA] maintained at 1, relaxation times of their corresponding dcFCCS curves increased (Fig. 1A and B), indicating that large condensates were formed at high concentrations and presented long residence times within the confocal detection volume. Based on our previous procedure (details in method section) (42), relaxation times of dcFCCS curves were extracted, from which the hydrodynamic radii of condensates were quantified (Fig. 1C; Figure S2A–C, Supplementary Material). When concentrations of FL-cGAS were 0.5 nM and 1 nM, the hydrodynamic radii of cGAS–DNA heterocomplexes were 8 nm and 20 nm, respectively, and remained almost constant over time (Figure S2D, Supplementary Material). Under these conditions, the proportions of AF488-FL-cGAS and Cy5-DNA interacting with each other, roughly estimated by the ratio of amplitude of dcFCCS curve (A_x) to amplitudes of autocorrelation curves of Cy5 channel (A_{640}) and AF488 channel (A_{488}), respectively, were very low (~10%; Fig. 1D and E; Figure S2A–C, Supplementary Material). Therefore, most FL-cGAS and DNA remained in the diluted phase under these low concentrations. When FL-cGAS reached 2 nM, nanoscale condensates were formed and growth rate of condensates accelerated over time (Fig. 1C–E; Figure S2D, Supplementary Material). When concentrations of FL-cGAS were 5 nM or higher, radii of condensates did not change significantly within our 5-min observation, suggesting the formation and growth of condensates mainly occurred within the initial 2-min period after sample mixing and before data collection (Figure S2E, Supplementary Material). In addition, the vast majority of FL-cGAS and DNA participated in condensates when concentrations of FL-cGAS were 2 nM or higher suggesting that 2 nM may serve as the critical concentration of FL-cGAS to form condensates with 99 bp DNA (Fig. 1C–E). To be visible by the conventional fluorescence microscope, concentrations of FL-cGAS had to be 20 nM or higher to form large condensates (Fig. 1C; Figure S1E and F, Supplementary Material). Consistent with our previous report, the dcFCCS method enables us to capture nanoscale condensates formed at the concentration an order of magnitude lower than the one defined by commonly used fluorescence microscopy.

Then, dcFCCS measurements were performed by varying concentrations of AF488-FL-cGAS and 99 bp Cy5-DNA from 0.5 to 200 nM independently. Total 81 different combinations of concentrations were used. Radii of heterocomplexes and condensates formed under these conditions were quantified and plotted in a 2D diagram (Fig. 1F). Clearly, high cGAS and DNA concentrations led to formation of large condensates. The critical concentrations to form nanoscale condensates (radius > 70 nm) were 2 nM for FL-cGAS and 1 nM for 99 bp DNA. In the presence of 10 nM FL-cGAS, close to physiological concentration, the radii of condensates were in the range of 100 to 250 nm with different DNA concentrations. With a close-to-physiological buffer condition containing 150 mM NaCl, the electrostatic interactions between cGAS and DNA were attenuated, which reduced the radii of condensates (Figure S3A–C,

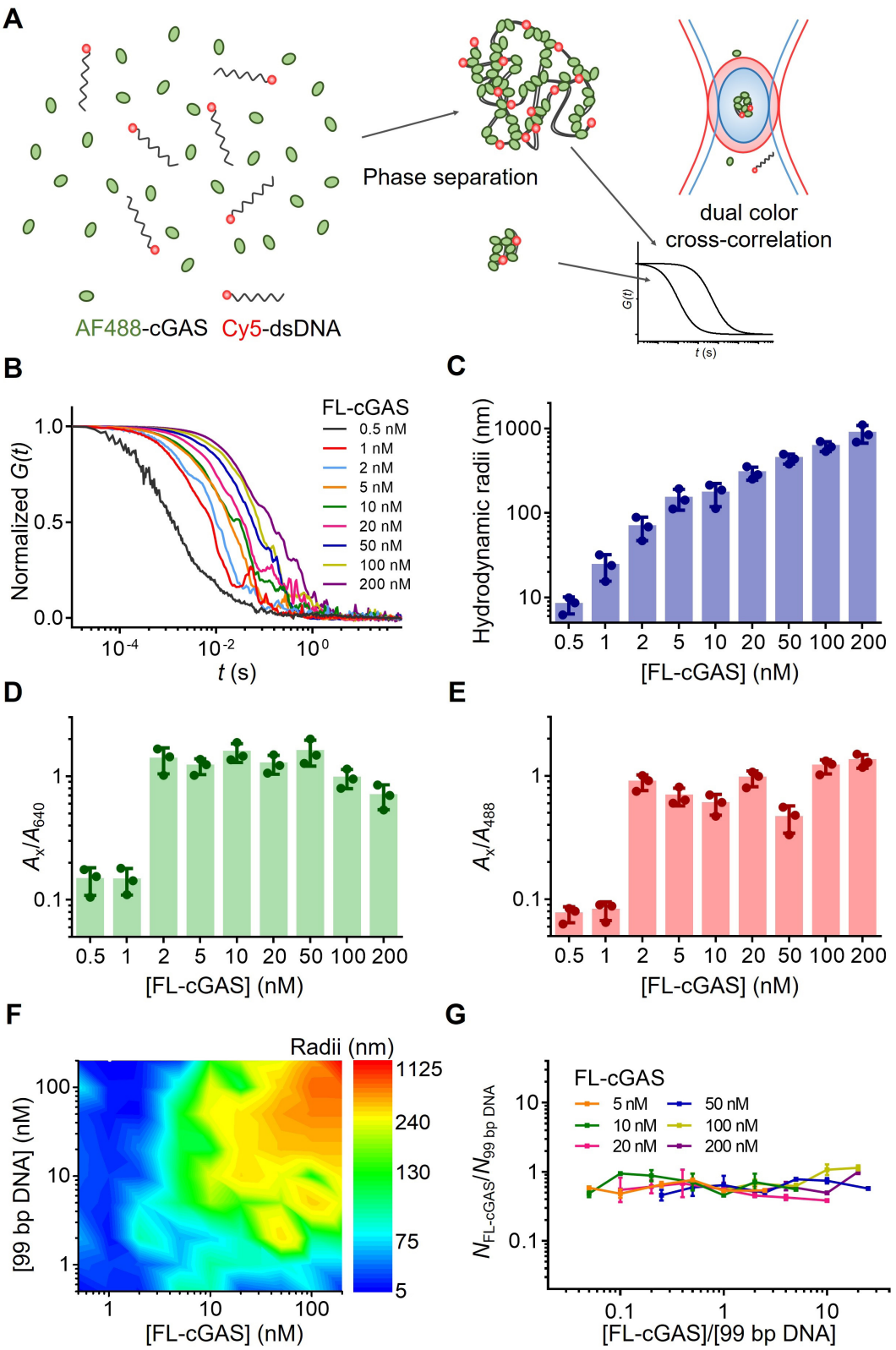

Fig. 1. Quantifying cGAS–DNA condensates at the nanoscale by dcFCCS. (A) Schematic diagram of dcFCCS assay. AF488-cGAS (green ovals) and Cy5-dsDNA (black helixes with red dots) diffuse through the excitation volume of 488 and 640 nm lasers. Only complexes and condensates carrying both AF488-cGAS and Cy5-dsDNA contribute to cross-correlation curves, whose relaxation times correlate with their sizes. (B) Normalized dcFCCS curves of condensates formed by AF488-FL-cGAS and 99 bp Cy5-DNA. 0.5 to 200 nM FL-cGAS were used as indicated. The initial [FL-cGAS]/[99 bp DNA] maintained constant at 1. (C) Hydrodynamic radii of condensates derived from dcFCCS curves shown in (B). (D)–(E) A_x/A_{640} (D) and A_x/A_{488} (E) roughly estimating proportions of FL-cGAS and DNA participating in condensates, respectively, under indicated cGAS concentrations (details in the Methods section). (F) 2D diagram of cGAS–DNA radii under indicated FL-cGAS and 99 bp concentrations. (G) Relation between cGAS:DNA stoichiometry in condensates and the initial concentration ratio of cGAS:DNA when [FL-cGAS] are 5 nM and higher. Color code is based on [FL-cGAS]. Data are presented as mean ± SD ($N = 3$), with individual points plotted in bar graphs.

Supplementary Material). Nevertheless, 45-nm condensates were formed and the majority of cGAS participated in condensation when 10 nM cGAS was used. Therefore, the high sensitivity provided by the dcFCCS method revealed that nanoscale condensates can form between DNA and cGAS at the endogenous expression level, whereas previous studies usually examined condensates formed from high concentrations of purified cGAS *in vitro* or overexpressed cGAS *in vivo* at the micronscale (30, 31).

The molecular stoichiometry of AF488-FL-cGAS and Cy5-DNA within condensates was quantified from the ratio of AF488:Cy5 intensities in the sparsely distributed fluorescence bursts after correcting FRET efficiency between AF488 and Cy5, which were generated when cGAS–DNA condensates randomly diffused through the excitation volume (Figure S4A–D, Supplementary Material). Interestingly, when the initial [AF488-FL-cGAS]/[Cy5-DNA] varied over two orders of magnitude from 0.05 to 20, the molecular stoichiometries of AF488-FL-cGAS and 99 bp Cy5-DNA within condensates remained almost constant around 0.5, corresponding to one FL-cGAS protein per two 99 bp DNA within the condensed phase (Fig. 1G; Figure S4E, Supplementary Material). Together, our results revealed that molecular composition within the condensed phase formed by FL-cGAS and 99 bp DNA is insensitive to their concentration ratio in the diluted phase. The condensed phase exhibits as an excellent buffer zone to provide a robust microenvironment. Furthermore, we revealed the salt concentration is able to regulate the molecular composition within the condensed phase (Figure S3D, Supplementary Material).

Condensate formation affected by DNA length

Structure of cGAS–DNA complex shows that their interaction interfaces cover about 10 bp on dsDNA. However, biochemical assays have shown that short DNAs (10 to 25 bp) are unable to elicit activity of cGAS, whereas long DNAs (> 45 bp) are needed to activate cGAS and to stimulate innate immunity with high efficiency (24, 27, 30, 39, 44). LLPS driven by multivalent interactions between cGAS and long DNAs has been proposed as the key element to activate cGAS (30). Herein, we designed a series of Cy5-DNAs (15 to 600 bp, DNA sequences in Table S3 (Supplementary Material)) and quantified properties of phase-separated condensates between them and AF488-FL-cGAS (Fig. 2A–D). In our experiments, at the same FL-cGAS concentration, the concentration of base pair (bp) remained constant among DNAs of different length. Thus, the initial [FL-cGAS]/[bp] kept constant at 1/50.

Overall, high concentrations of FL-cGAS and DNA led to forming large cGAS–DNA heterocomplexes and condensates and long DNAs were more prone to form phase-separated condensates with FL-cGAS than short DNAs (Fig. 2A). For instance, the FL-cGAS concentrations needed to form ∼50 nm condensates with 15 bp, 20 bp, 25 bp, 45 bp, 99 bp, 300 bp, and 600 bp DNAs were approximately 200 nM, 200 nM, 50 nM, 20 nM, 2 nM, 1 nM, and 1 nM, respectively. For long dsDNAs (≥ 45 bp), these concentrations were likely to be the critical concentrations for the corresponding DNAs to induce formation of nanoscale condensates. When above the critical concentrations, almost all DNAs participated in the condensed phase, indicated by the values of A_x/A_{488} close to or above 1 (Fig. 2C). Because the molar ratios of [FL-cGAS] to [bp] within the condensates were around 1/100 to 1/500 (Fig. 2D), which were smaller than [FL-cGAS]/[bp] (1/50) used to initiate LLPS, a significant portion of FL-cGAS remained in the diluted phase, indicated by the values of A_x/A_{640} in the range of 0.2 to 0.8 (Fig. 2B). In total, two 45 bp DNAs of different sequences displayed similar behaviors (Figure S5A–C, Supplementary Material), confirming that interactions between cGAS and DNA to promote condensates formation are DNA sequence-independent (23, 45).

The stoichiometries of AF488-FL-cGAS and Cy5-DNA within condensates were ∼0.5 for 45 and 99 bp DNAs, ∼0.8 for 300 bp DNA, and ∼1.5 for 600 bp DNA (Fig. 2D). The overall trend was reasonable, as each long DNA molecule can interact with more cGAS molecules than short one. Consistent with our previous findings (Fig. 1G), the stoichiometries of AF488-FL-cGAS and Cy5-DNA remained almost constant while their initial concentrations and concentration ratios changed over two orders of magnitude (Fig. 2D; Figure S5D and E, Supplementary Material). Also, the values of stoichiometry were insensitive to DNA sequence (Figure S5D and E, Supplementary Material). Next, we applied fluorescence imaging based approach to quantify concentrations of AF488-FL-cGAS and Cy5-DNA within micronscale condensates formed at high concentrations (Figure S6A–D, Supplementary Material). Interestingly, FL-cGAS was always enriched to ∼16 μM within the condensates regardless of the DNA length and salt concentration, whereas DNAs were enriched to 10 to 32 μM depending on their length (Fig. 2E; Figure S3E, Supplementary Material). Although imaging-based approach cannot quantify concentrations within nanoscale condensates beyond the optical diffraction limit, the ratios of AF488-FL-cGAS and Cy5-DNA within nanoscale condensates determined by dcFCCS agreed with the ratios within micronscale condensates measured by imaging method, which confirmed the accuracy of these measurements (Figure S6E, Supplementary Material). In summary, our results revealed that condensation of FL-cGAS and DNA provides a stable buffering zone to maintain FL-cGAS at ∼16 μM regardless of the DNA length, salt concentration, the initial concentrations of FL-cGAS and DNA, and their concentration ratio.

Binding affinities with ATP/GTP and activities of cGAS affected by DNA of different length

Previous studies have suggested that interactions between cGAS and DNA in the absence of phase separation is insufficient to activate cGAS and to permit cGAMP production (30). Herein, we speculated whether phase-separation-induced condensation enhances binding affinities of substrates to promote cGAS activities. To this end, we aimed to quantitatively examine how binding affinities of cGAS with substrates (ATP and GTP) and cGAMP production are affected by DNA binding in the absence and presence of condensation, respectively. Short DNAs could not form large condensates with FL-cGAS at low concentration (< 10nM for 25 bp DNA and < 50 nM for 15- and 20 bp DNAs), permitting us to use dcFCCS to quantify binding affinities (K_d) of FL-cGAS with 15 bp, 20 bp, and 25 bp DNAs as 590 ± 190 nM, 300 ± 70 nM, and 150 ± 20 nM, respectively (Fig. 2F; Figure S7A, Supplementary Material). Therefore, a mixture of FL-cGAS with 5 μM 15 bp DNA was used to represent DNA-bound cGAS in the absence of condensation (Fig. 2G and H).

The binding affinities of ATP with FL-cGAS in the apo and DNA-bound state were 5.6 ± 0.4 μM and 4.5 ± 0.9 μM, respectively (Fig. 2G; Figure S7B and C, Supplementary Material), whereas the binding affinities of GTP with FL-cGAS in both the apo and DNA-bound state were beyond the detection limit of our dcFCCS method (> 50 μM; Figure S7E and F, Supplementary Material). On the other hand, phase-separation induced condensation greatly enhanced the binding affinities of cGAS with ATP and GTP, which were ∼2 μM and 3–4 μM, respectively, when 45 to 600 bp DNAs were used (Fig. 2G; Figure S7D and G, Supplementary Material). In addition, FL-cGAS in the apo and DNA-bound state were

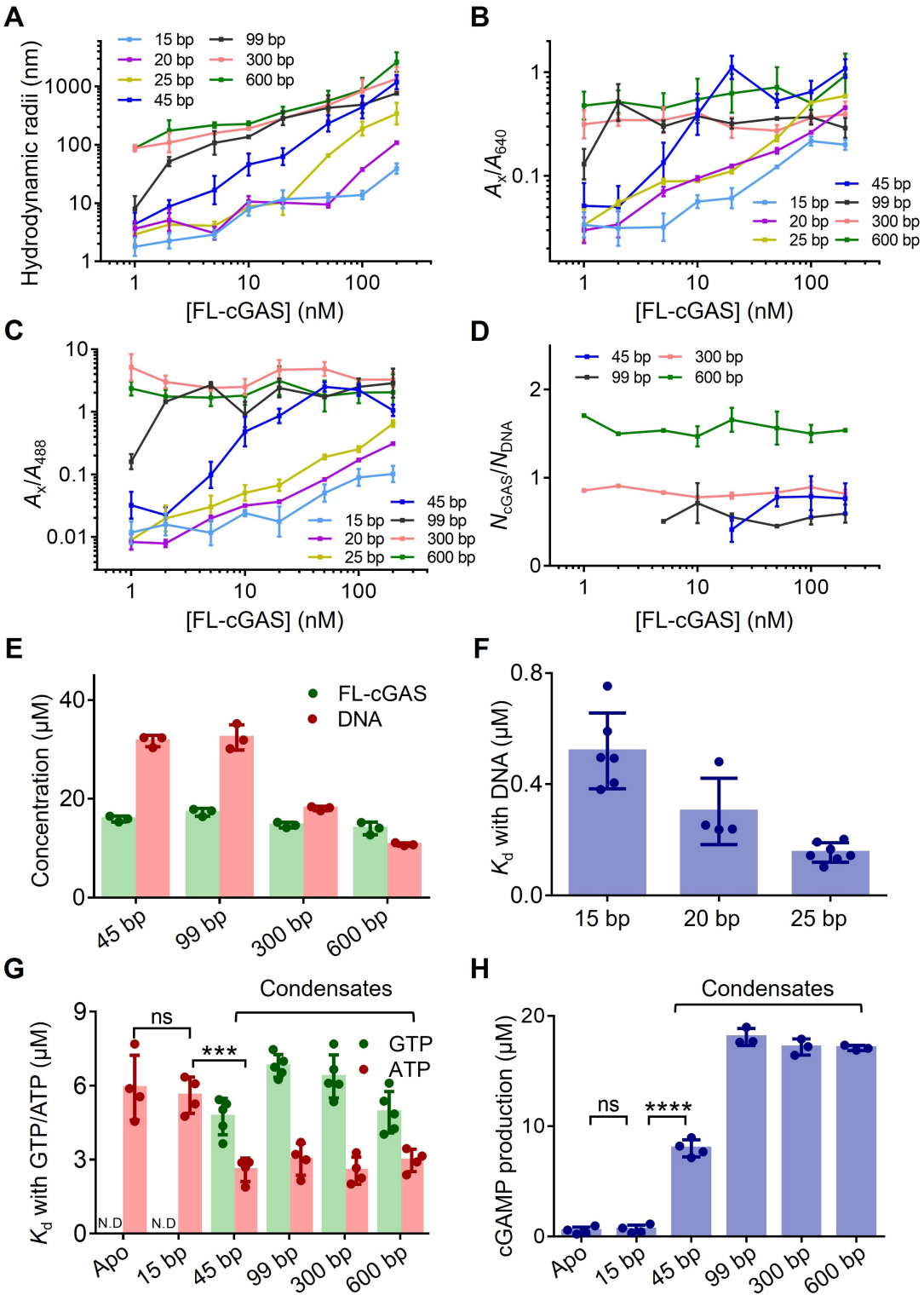

Fig. 2. Quantifying condensates formed from cGAS and DNA of different length. (A) Hydrodynamic radii of condensates formed from FL-cGAS and DNA of different length, which varies from 15 to 600 bp. The initial [FL-cGAS]/[bp] maintained constant at 1/50. (B) and (C) A_x/A_{640} (B) and A_x/A_{488} (C) roughly estimating proportions of FL-cGAS and DNA participating in condensates, respectively, with DNA of different length under different concentrations. (D) Stoichiometries of FL-cGAS and DNA of different length within condensates under indicated concentrations. (E) Concentrations of FL-cGAS (green) and DNA (red) within condensates quantified via TIRF imaging based assays (Figure S6A–D, Supplementary Material). Condensates were formed from 100 nM FL-cGAS with 110 nM 45 bp DNA, 50 nM 99 bp DNA, 16.5 nM 300 bp DNA, or 8.3 nM 600 bp DNA. (F) Binding affinities of FL-cGAS with 15, 20, and 25 bp DNAs. (G) Binding affinities of FL-cGAS under different conditions with substrates GTP (green) and ATP (red). The experiments were carried out when FL-cGAS were at the apo state, the DNA-bound state in the absence of phase separation (with 5 μM 15 bp DNA) and condensed states formed with DNA of different length. 100 nM cGAS and 100 nM labeled GTP/ATP were used in all conditions. Concentrations of DNA were the same as (E). (H) cGAMP production of 100 nM FL-cGAS under different states as shown in (G). Data are presented as mean ± SD ($N = 3$), with individual points plotted in bar graphs. Statistical significance was assessed by two-tailed unpaired t test in (G) and (H). Statistical differences were represented as follows: ns not significant, *** $P < 0.001$ and **** $P < 0.0001$.

unable to produce cGAMP, whereas phase separation of FL-cGAS with long DNAs activated cGAMP production (Fig. 2H; Figure S8A, Supplementary Material). Decreasing concentration of FL-cGAS from 200 to 10 nM had almost no influence on cGAMP production per cGAS molecule, whereas increasing concentration of NaCl from 100 to 150 mM reduced cGAS activity by ∼50% (Figure S8B–E, Supplementary Material). Together, our results showed that DNA binding induced condensation not only activates FL-cGAS but also enhances its binding affinities with ATP and GTP by ∼3- and > 10-fold, respectively, whereas DNA binding alone without condensation is insufficient to enhance ATP/GTP binding and cGAMP production. Next, we aimed to further examine whether enhanced binding affinities of substrates within condensates generally correlate with the promoted cGAS activities.

Condensate formation, ATP/GTP recruitment, and cGAMP production of cGAS variants

Phase separation of cGAS was mediated via multivalent interactions between cGAS and DNA. FL-cGAS has four DNA binding sites, including three positive-charged surfaces, named sites A, B, and C, respectively, and a positive-charged intrinsically disordered N-terminal tail (23, 29, 38, 46–49). In addition, once binding to DNA, cGAS assembles into a complex containing two cGAS molecules and two DNA molecules via a dimerization interaction site (29, 49). Previous studies have shown that all of these interaction sites (residues summarized in Table S4 (Supplementary Material)) were important for phase separation and activation of cGAS (10). Here, we generated a series of cGAS variants to disrupt these important interaction sites contributing to multivalent interactions, which included Δ160-cGAS (N-terminal truncated), cGAS-K394A (dimer interface mutated), cGAS-K384E (site A mutated), cGAS-K347E (site B mutated), and cGAS-K427E/K428E (site C mutated; Fig. 3A and B; Figure S9A, Supplementary Material). In addition, we generated the cGAS-K187N/L195R variant, which contained two mutations within the site A and was reported to sense short DNA, to induce high-order oligomerization of cGAS and to enhance cGAS activity *in vitro* and *in vivo* (50, 51). To test our hypothesis raised above, we applied dcFCCS to quantify how condensation is affected by cGAS mutations to modulate cGAS activities.

First of all, we quantified binding affinities of these cGAS mutants with 25 bp DNA (Fig. 3C). Among them, Δ160-cGAS presented the weakest binding affinity (K_d ∼2 μM), which was ∼10-fold weaker than FL-cGAS. cGAS-K427E/K428E exhibited ∼2-fold weaker binding affinity than FL-cGAS, whereas GAS-K394A, cGAS-K384E, and cGAS-K347E displayed similar K_d with DNA as FL-cGAS. Binding affinity of cGAS-K187N/L195R with DNA was slightly stronger than FL-cGAS. To quantify binding affinity between DNA and each DNA binding sites, we constructed a cGAS mutant (Δ160-cGAS$_{4M}$) based on cGAS$_{4M}$ (cGAS-K394A/K384E/K347E/K427E/K428E) with sites A, B, C and the dimerization interaction site mutated and N-terminal truncated. Δ160-cGAS$_{4M}$ presented the lowest binding affinity (K_d ∼4 μM, Fig. 3D) with 25 bp DNA. When one of these mutated or truncated sites was restored to their original sequences, the binding affinity between cGAS variant and DNA increased (Fig. 3D). Together, these results indicated that the N-terminal tail is the strongest DNA binding site (K_d ∼0.5 μM), whereas the binding between DNA and other sites (sites A, B, and C) are weak with K_d ∼2 μM.

Next, condensate formation between the cGAS variants and 99 bp DNA under different concentrations was examined (Fig. 3E–G). In general, the abilities of cGAS variants to form phase separation were strongly correlated with their binding affinities with DNA. Condensation of Δ160-cGAS was attenuated the most. Even at the highest concentration we tested (200 nM), ∼50% of Δ160-cGAS remained in the diluted phase and the radius of cGAS–DNA heterocomplex was ∼100 nm, while the condensate of FL-cGAS reached micronscale at the same concentration. For cGAS-K394A, cGAS-K384E, cGAS-K347E, and cGAS-K427E/K428E containing mutations to disrupt dimer interface, site A, site B, and site C, respectively, their critical concentrations, above which the majority of cGAS variants participated in the condensed phase, were ∼10 nM and 5-fold higher than FL-cGAS (2 nM; Fig. 3E–G). They also formed smaller cGAS–DNA heterocomplexes and condensates than FL-cGAS at low concentration (Fig. 3E). Under most concentrations, cGAS-K187N/L195R displayed similar behaviors as FL-cGAS. However, at the lowest concentration we tested (1 nM), condensate formed from cGAS-K187N/L195R was larger and its proportions of cGAS and DNA within the condensed phase were higher than FL-cGAS. In addition, when 45 bp DNA was used, cGAS-K187N/L195R was more prone to participate in the condensed phase and to form larger condensates than the FL-cGAS (Figure S9B–D, Supplementary Material).

Then, we quantified the molecular stoichiometry with the condensates and the abilities of cGAS variants to recruit ATP and GTP. The ratio of cGAS and 99 bp DNA remained around 0.5 confirmed by both dcFCCS and imaging methods, no matter which cGAS variants were used (Fig. 3H; Figure S9E, Supplementary Material). However, the local concentrations of cGAS and DNA within the condensates were highly affected by protein mutations (Fig. 3I). Concentrations of cGAS variants in the condensed phase were strongly correlated with their binding affinities with DNA. Particularly, the concentrations of Δ160-cGAS and cGAS-K427E/K428E, which presented weak binding with DNA, were ∼7-fold and ∼5-fold lower than the FL-cGAS, respectively. On the other hand, the abilities of cGAS to recruit ATP and GTP in their apo state and in the condensed phase were only moderately affected by the N-terminal truncation and protein mutations we tested (Fig. 3J; Figure S9F, Supplementary Material). There were two exceptions. cGAS-K187N/L195R presented the highest binding affinity with GTP (K_d ∼1 μM), enhanced 4-fold compared with FL-cGAS. On the other hand, the binding between GTP and Δ160-cGAS in the condensed phase was greatly reduced, whose K_d was beyond the detection limit (> 50 μM) of our dcFCCS assay.

Lastly, cGAMP production of cGAS variants after condensation was quantified (Fig. 3K; Figure S9G, Supplementary Material). Consistent with previous reports, cGAS-K187N/L195R produced more cGAMP than the FL-cGAS, whereas Δ160-cGAS synthesized slightly less cGAMP than the FL-cGAS. The activities of the other four cGAS variants were completely abolished, although all of them displayed higher DNA and ATP/GTP binding affinities and better condensation formation than Δ160-cGAS. Our results clearly invalidated the hypothesis raised above and indicated that enhanced cGAS activities are not caused by enhanced binding affinities of ATP/GTP. Instead, the essential roles of DNA binding sites A, B, and C and the dimer interface in activating cGAS are emphasized, even in the presence of phase-separated condensation.

Effect of Zn^{2+}, Mn^{2+}, and RNA on condensate formation and activity of cGAS

To provide a quantitative comprehensive view to elucidate the role of condensate formation in cGAS activation, we examined effect of Zn^{2+}, Mn^{2+}, and RNA. Clearly, the presence of either

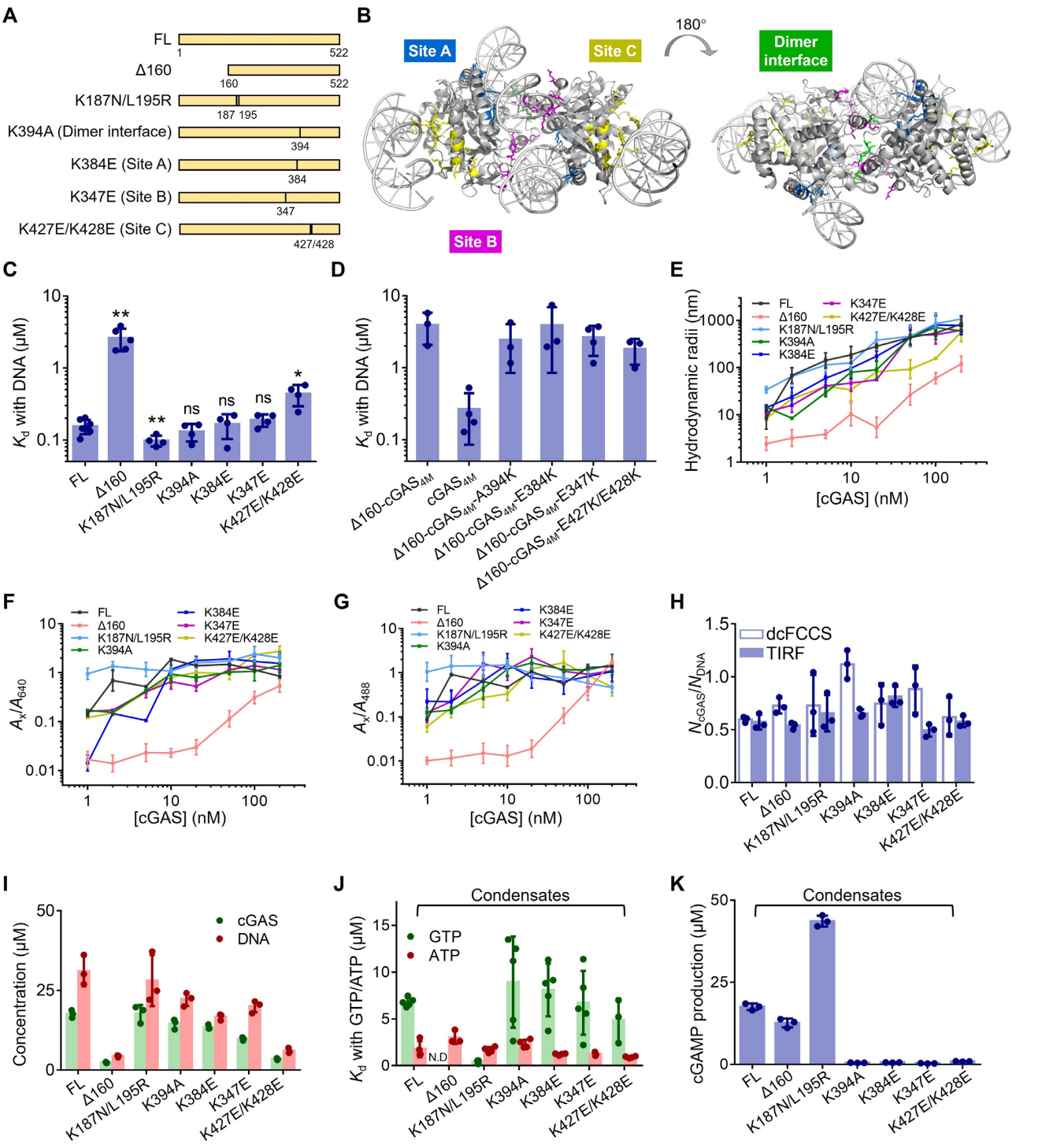

Fig. 3. Quantifying condensates formed from cGAS variants. (A) Scheme of FL-cGAS and mutants. (B) Structure of cGAS–DNA heterocomplex. Site A (blue), site B (magenta), site C (yellow), and dimer interface (green) were colored. The structure information was superimposed from PDB 4LEV, 4LEY, and 6EDB. The specific sites were summarized from previous reports and shown in Table S4 (Supplementary Material) (29, 49, 51). (C) Binding affinities of cGAS variants with 25 bp DNA. (D) Binding affinities of cGAS variants with 25 bp DNA. $cGAS_{4M}$: cGAS-K394A/K384E/K347E/K427E/K428E with DNA binding sites A, B, and C and dimerization interaction site mutated; Δ160-$cGAS_{4M}$: N-terminus truncated $cGAS_{4M}$; Δ160-$cGAS_{4M}$-A394K: dimerization site restored from Δ160-$cGAS_{4M}$; Δ160-$cGAS_{4M}$-E384K: site A restored from Δ160-$cGAS_{4M}$; Δ160-$cGAS_{4M}$-E347K: site B restored from Δ160-$cGAS_{4M}$; and Δ160-$cGAS_{4M}$-E427K/E428K: site C restored from Δ160-$cGAS_{4M}$. (E) Hydrodynamic radii of cGAS–DNA condensates formed under indicated cGAS concentrations. A length of 99 bp DNA was used to interact with FL(black), Δ160 (red), K187N/L195R (cyan), K394A (green), K384E (blue), K347E (magenta), and K427E/K428E (yellow). The initial [cGAS]/[99 bp DNA] maintained constant at 1. (F) and (G) A_x/A_{640} (F) and A_x/A_{488} (G) roughly estimating proportions of cGAS and DNA participating in condensates, respectively. (H) Stoichiometries of cGAS and 99 bp DNA within condensates quantified by dcFCCS method (open) and TIRF imaging-based assays (solid). (I) Concentrations of cGAS (green) and 99 bp DNA (red) quantified via TIRF imaging-based assays. (J) Binding affinities of cGAS variants with substrates GTP (green) and ATP (red) in their condensed state. A total of 100 nM labeled GTP/ATP were used. (K) cGAMP production of cGAS variants in their condensed state. A total of 100 nM cGAS was used to form condensates with 100 nM 99 bp DNA in (H), (I), (J), and (K). Data are presented as mean ± SD ($N = 3$), with individual points plotted in bar graphs. Statistical significance was assessed by two-tailed unpaired t test in (C). Statistical differences were represented as follows: ns not significant, * $P < 0.1$ and ** $P < 0.01$.

Zn^{2+} or Mn^{2+} greatly enhanced the phase separation of cGAS and DNA, which was indicated by the formation of ∼100 nm condensates even in the presence of 1 nM FL-cGAS (Fig. 4A–C). However, condensate formation was moderately attenuated when double-stranded RNA (dsRNA) was used to replace dsDNA (Fig. 4A–C; RNA sequence in Table S3 (Supplementary Material)). The molecular stoichiometries of FL-cGAS and DNA (or RNA) and the concentration of FL-cGAS within condensates remained almost constant in the presence of Zn^{2+}, Mn^{2+}, and RNA, respectively (Fig. 4D and E; Figure S10A, Supplementary Material). In the apo state, Mn^{2+} slightly enhanced binding affinity between FL-cGAS and ATP, whereas the binding between FL-cGAS and GTP was still beyond our detection limit. Consistent with our results above (Fig. 2G), FL-cGAS in the condensed phase, in the presence of Zn^{2+}, Mn^{2+}, or RNA, all displayed stronger binding affinities with GTP and ATP than FL-cGAS in the apo state (Fig. 4F). However, consistent with previous reports (26, 30, 52–54), both Zn^{2+} and Mn^{2+} enhanced cGAMP production after DNA-induced condensation, whereas condensates formed from FL-cGAS and RNA had no detectable activities (Fig. 4G; Figure S10B, Supplementary Material). Mn^{2+} was able to activate FL-cGAS in the apo state (Fig. 4G; Figure S10B, Supplementary Material). Clearly, condensation and enhanced ATP/GTP recruitment are not necessary and not sufficient to activate cGAMP production.

cGAS activation in the absence of phase separation

Our results confirmed previous reports that DNA binding sites A, B, and C and the dimer interface are all essential sites to activate cGAS (Fig. 3B). Mutations in these essential sites completely abolish cGAS activities while only mildly attenuate condensation, whereas the N-terminal truncated cGAS exhibits greatly reduced condensation with mildly affected activity (Fig. 3). Our quantitative comparison strongly supports that the activation of cGAS is directly mediated by interactions at these essential sites, not directly caused by phase-separation-induced condensation.

Our measurements showed that binding affinities between DNA and these three essential DNA binding sites were weak with K_d ∼2 μM (Fig. 3D). In addition, the apparent binding affinity between FL-cGAS monomers to form cGAS dimer was ∼2 μM in the absence of DNA and decreased to ∼400 nM when 5 μM of 15 bp DNA was added (Fig. 5A). However, the physiological concentration of cGAS in cell (∼10 nM (30)) is 1 to 2 orders of magnitude lower than binding affinities of these essential sites, suggesting that, in the absence of phase separation, most of these sites would be unbound so that the majority of cGAS remained in its inactive apo state. We hypothesized that the function of cGAS–DNA phase separation is to provide enriched cGAS and DNA local concentrations (>10 μM, Fig. 2E) within the condensed phase, which are significantly higher than binding affinities of these essential sites. Therefore, within the condensates, DNA binding sites A, B, and C and the dimer interface are mostly bound with their partners, inducing the activation of cGAS and cGAMP production.

Our hypothesized model provided the fundamental molecular mechanism of cGAS activation and a rational explanation why condensate formation is necessary but not sufficient to activate cGAS in the absence of Mn^{2+}. To validate our model, we further engineered cGAS to activate it in the absence of phase separation. Within all three conditions we tested, 100 μM 15 bp DNA and 100 nM FL-cGAS or glutathione transferase (GST) tag-fused cGAS (GST–cGAS) were used (Fig. 5B and C). The concentration of 15 bp DNA was 50-times higher than binding affinities to fully occupy DNA binding sites A, B, and C. However, the concentration of FL-cGAS was significantly lower than the binding affinity between FL-cGAS monomers, resulting in low level of dimerization and almost no cGAMP production. When crowding reagent (20% polyethylene glycol-8000, PEG8000) was added to facilitate formation of 50 nm radius cGAS–DNA heterocomplexes, dimerization of cGAS is likely to be promoted due to high local concentration within the heterocomplexes, leading to a significant boost in cGAMP production. To further minimize the size of heterocomplexes of cGAS–DNA while inducing dimerization of cGAS, a GST tag was fused to the N terminal of cGAS. The GST tag is known to form dimer at 1 nM or lower (55). The size-exclusion chromatography and fluorescence correlation spectroscopy (FCS) measurements confirmed the dimerization of GST–cGAS (Figure S11A and B, Supplementary Material), which would facilitate interactions between two cGAS monomers via their authentic dimer interface. Consistent with our expectation, GST–cGAS only formed 10 nm radius heterocomplexes in the presence of 100 μM 15 bp DNA while exhibiting high activity (Fig. 5B and C). We further decreased concentration of GST–cGAS to 10 nM to reduce the probability to form GST–cGAS tetramer and heterocomplexes. Using buffer containing 100 mM or 150 mM NaCl, 10 nM GST–cGAS with 15 bp DNA with reduced radii displayed similar activity as FL-cGAS with 99 bp DNA (Figure S11C and D, Supplementary Material). Under these conditions, conventional fluorescence microscopy could not capture any sign of phase separation (Figure S11E, Supplementary Material). Together, we not only activate cGAS using 15 bp short DNA in the absence of phase separation, but also validate our mechanistic model in which the activation of cGAS is mediated by binding of cGAS sites A, B, and C and the dimer interface with their correct partners (Fig. 5D–H).

Discussion

As the key element of the cGAS–STING pathway and an innate immune system response to protect cells from viral or microbial infection or self-DNA (13, 20), cGAS functions as an initial DNA sensor to synthesize the second messenger cGAMP, which activates STING and further induces the production of interferon (1, 8–10). Dysregulation or loss of function of cGAS are known to associate with inflammatory, autoimmune disease, or tumorigenesis (56–58). Due to the essential role of cGAS in the immune system, many structural, biochemical, and cellular studies have been conducted to shed lights on its molecular mechanisms. Binding of DNA with cGAS induces its catalytic pocket to undergo a structural rearrangement to permit cGAMP synthesis (26, 27). In addition, DNA and cGAS can form oligomers and micronscale condensates through LLPS, which promotes activation of cGAS and mounts a robust immune defense (26, 29, 30). Several coreceptors were demonstrated to promote the cGAS-mediated innate immune response via dramatically enhancing oligomerization and condensation of cGAS–DNA (59–61). On the other hand, several viral proteins were reported to inhibit formation of cGAS–DNA condensates and to suppress the antiviral innate immune response (31, 62, 63). Together, these studies conclude that DNA binding induces conformational change and phase-separation-induced condensation of cGAS *in vivo* to activate and to promote cGAMP production, respectively.

Despite all these researches, the molecular mechanisms of condensation to enhance cGAMP production of cGAS remain unknown. A recent study revealed that, although diverse vertebrate cGAS homologs can all form condensates with DNA under certain

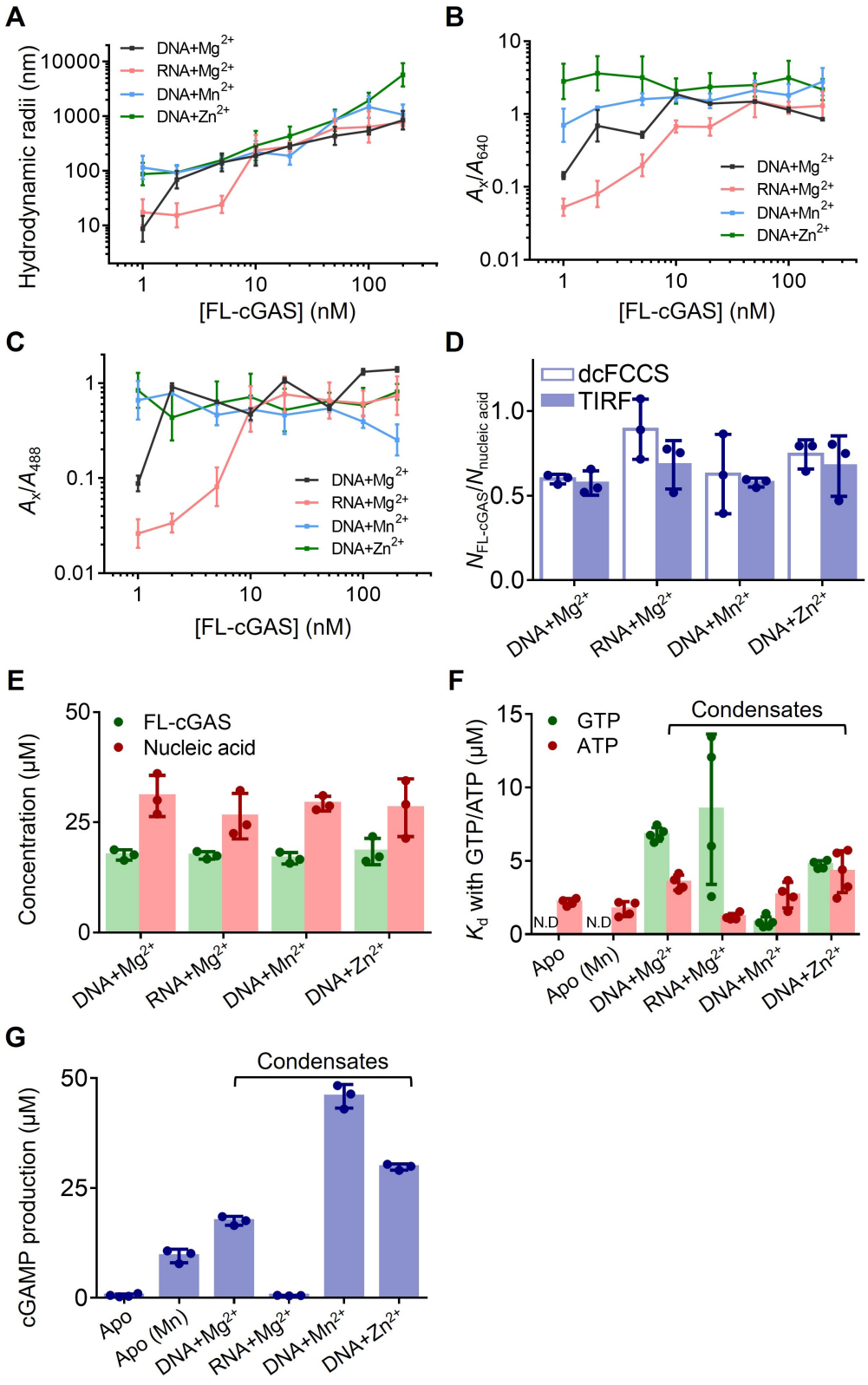

Fig. 4. Effect of Zn^{2+}, Mn^{2+}, and RNA on phase separation, substrate binding affinities and activity of cGAS. (A) Hydrodynamic radii of condensates in the presence of DNA with Mg^{2+} (black), Mn^{2+} (blue), or Zn^{2+} (green) or in the presence of RNA with Mg^{2+} (red). (B) and (C) A_x/A_{640} (B) and A_x/A_{488} (C) roughly estimating proportions of FL-cGAS and nucleic acid participating in condensates, respectively, under indicated concentrations and experimental conditions. The initial [cGAS]/[99 bp DNA or RNA] maintained constant at 1. (D) Stoichiometries of FL-cGAS and nucleic acid within condensates detected by dcFCCS method (open) and TIRF imaging-based assays (solid). (E) Concentrations of cGAS (green) and nucleic acid (red) under indicated conditions. (F) Binding affinities of cGAS with GTP (green) and ATP (red) under indicated conditions. Experiments were carried out with cGAS in the apo state and the condensed states. (G) cGAMP production under indicated conditions. A total of 100 nM cGAS was used to form condensates with 100 nM 99 bp dsDNA or 100 nM 99 bp dsRNA in (D), (E), (F), and (G). A total of 5 mM Mg^{2+}, 5 mM Mn^{2+}, or 200 μM Zn^{2+} were added in buffer (20 mM Tris-HCl pH 7.5, 100 mM NaCl) separately. Data are presented as mean ± SD ($N = 3$), with individual points plotted in bar graphs.

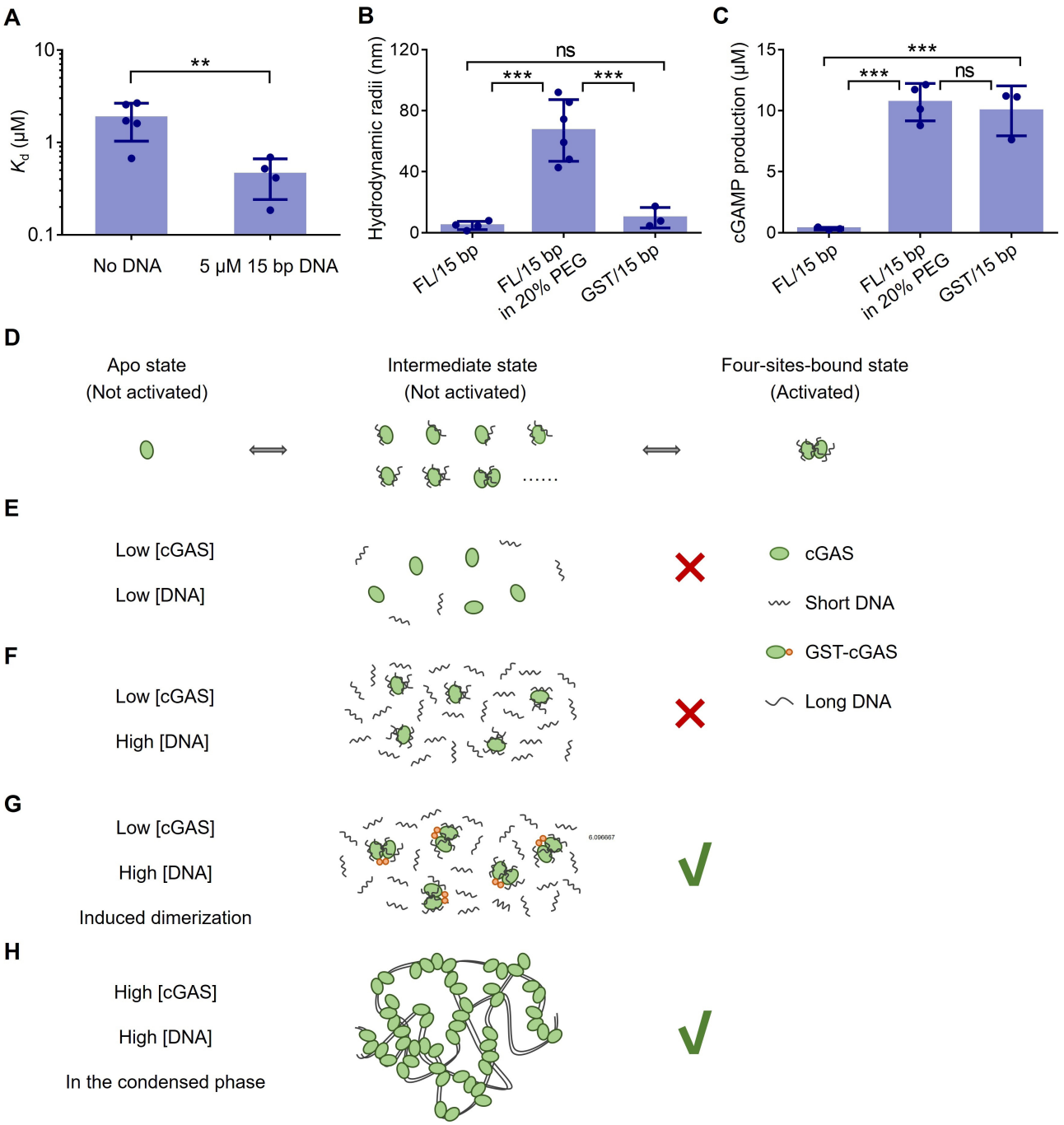

Fig. 5. cGAS activation in the absence of phase separation. and the proposed mechanistic model. (A) Apparent binding affinities between FL-cGAS monomer to form dimer without or with 5 μM DNA. (B) and (C) Hydrodynamic radii (B) and cGAMP production (C) of cGAS–DNA heterocomplexes formed from 100 μM 15 bp DNA and 100 nM FL-cGAS or GST–cGAS. A total of 20% PEG8000 was used as a crowding reagent to facilitate formation of cGAS–DNA heterocomplexes. Glutathione transferase (GST) tag was fused to the N terminal of cGAS to induce dimerization. (D) Scheme of mechanistic model of cGAS activation. cGAS at the apo and intermediate states are not activated, while cGAS at the four-sites-bound state is activated. (E) Low concentration of cGAS and DNA lead to essential sites unbound, resulting in almost no activity. (F) Low concentration of cGAS with high concentration of DNA, leading to cGAS binding with DNA without dimerization, which also results in no activity. (G) Low concentration of GST–cGAS with high concentration of DNA, leading to the four-sites-bound state formation with activity. (H) In the condensed phase, cGAS and DNA are enriched to high concentration, leading to the four-sites-bound state formation with activity. Data are presented as mean ± SD (N = 3), with individual points plotted in bar graphs. Statistical significance was assessed by two-tailed unpaired t test in A, B, and C. Statistical differences were represented as follows: ns not significant, ** $P < 0.01$ and *** $P < 0.001$.

conditions, their cGAMP production has no direct relationship with condensate formation (41). Thus, they constructed a chimeric cGAS from human cGAS and mouse cGAS with a dramatic reduction in condensate formation while retaining activity to synthesize cGAMP. In addition, dsRNA is able to induce phase separation of cGAS without enzymatic activity. Together, these phenomena suggest that phase separation of cGAS is unlikely to directly contribute to cGAMP production. Here, with the highly sensitive dcFCCS method, we captured nanoscale cGAS–DNA condensates and quantified their molecular composition and binding

affinities, shedding light on molecular mechanisms of cGAS activation and the roles of phase separation in promoting activation.

Our study revealed that the critical cGAS concentration to form nanoscale condensates is ~2 nM, which is an order of magnitude lower than the critical concentration (30 to 50 nM) to form micron-scale condensates identified by conventional fluorescence microscopy in previous studies (Fig. 1C and E; Figure S1E and F, Supplementary Material), suggesting that cGAS expressed at the endogenous level (~10 nM) is sufficient to form condensates upon sensing DNA to activate cGAMP production (Figure S8B–E, Supplementary Material) and the downstream signal pathway. Unlike the engineered yeast SmF variants examined in our previous report showing linear growth of their condensates over time (42), 2 nM of FL-cGAS leads to accelerated increase of condensate radii indicating that cGAS and DNA induce fast LLPS (Figure S2D, Supplementary Material). When FL-cGAS concentration is 5 nM or higher, the major growth phase of phase-separated cGAS–DNA condensates completes within 2 min, suggesting that the response of the endogenous cGAS after sensing DNA is fast and occurs within several minutes (Figure S2E, Supplementary Material).

In structures of DNA–cGAS (27, 49, 64), each cGAS molecule interacts with three DNA molecules via sites A, B, and C, respectively, while forming a dimer with a nearby cGAS molecule. These interactions cooperatively promote LLPS, which is the previous proposed model to activate cGAS. Our results confirmed previous reports that interactions between DNA and cGAS at these DNA binding sites and the dimerization of cGAS are all necessary to activate cGAS (Fig. 3B and K). In addition, we further revealed that these interactions are sufficient and the fundamental molecular basis to fully activate cGAS, even in the absence of LLPS (Fig. 5). Hooy and Sohn established a model that dimerization of cGAS is essential for DNA-mediated activation, allosterically regulated by DNA in a length-dependent manner (44). Built on their model, we proposed that having cGAS dimerization and all these DNA binding sites occupied is sufficient and necessary to activate cGAS (Fig. 5D). Therefore, mutating any one of these indispensable sites would only mildly affect phase separation while completely abolishing cGAS activity. The binding affinities of these sites with their partners are relative weak (~2 μM, Figs 3D and 5A). When phase separation is not induced in the presence of short DNA, physiological concentrations of cGAS and DNA in the diluted phase are far below binding affinities of these sites, which leads to vacancy of these essential sites resulting almost no activity of cGAS (Fig. 5E). Even with high concentration of short DNA to fully occupy cGAS sites A, B, and C in the diluted phase, cGAS under close to physiological concentration cannot form dimers, whose binding constant is ~0.4 μM, resulting in almost no activity (Fig. 5F). On the other hand, in the presence of long DNA, the phase-separation-induced cGAS–DNA condensates provide an excellent buffering zone to enrich cGAS to ~16 μM (Fig. 2E), regardless of the DNA length, the initial concentrations of cGAS and DNA and their relative ratios, which are higher than binding affinities of these sites. Thus, these essential sites are mostly bound in the condensed phase, leading to enhanced cGAS activity (Fig. 5H).

Guided by our proposed model, we are able to activate cGAS in the absence of phase separation. GST tag, which is known to form dimer by itself, is fused onto the N-terminal of cGAS to facilitate interactions between two cGAS molecules via their authentic dimerization site. In addition, 100 μM of 15 bp short DNA, whose concentration is significantly higher than binding affinities of sites A, B, and C with DNA, is used to fully occupy these sites (Fig. 5G). Consistent with our design, GST–cGAS only forms 10-nm-radius heterocomplexes with DNA and displays no signal of LLPS while maintaining high cGAMP production activity (Fig. 5B and C; Figure S11E, Supplementary Material). Thus, our proposed model is further validated.

In our proposed model, the fundamental molecular basis to activate cGAS is to have its DNA binding sites A, B, and C and dimer interface bound, whereas phase separation mediated by DNA serves as an important auxiliary factor to increase local concentrations and to facilitate binding among cGAS and DNA molecules. Our model reconciles several experimental phenomena, in which the phase separation does not correlate with activity. Although phase separation and enrichment of cGAS and DNA are greatly reduced for Δ160-cGAS, Δ160-cGAS and DNA concentrations in the condensed phase are only decreased to ~2 μM and ~5 μM, respectively (Fig. 3I), which are still above the binding affinities of these key sites. Therefore, even in the absence of the N-terminus, these essential sites still mostly remain bound, leading to an activity close to FL-cGAS (Fig. 3K). dsRNA, an incorrect binding partner with DNA binding sites, can induce phase separation but cannot activate cGAS by itself (Fig. 4) (30). However, the cGAS–RNA condensates provide highly concentrated cGAS to facilitate binding between cGAS and DNA and dimerization of cGAS, which would enhance cGAS activity in the presence of low concentration of DNA as previously reported (65).

We also revealed that binding affinities of cGAS with its substrates, ATP and GTP, in the condensed phase are enhanced by ~3- and > 10-fold, respectively (Fig. 2G), which is likely caused by the reduced excluded volume in the condensed phase to enhance association of molecules (33, 66, 67). Because the concentrations of ATP and GTP in cells are ~1 mM (68), which are significantly higher than their binding affinities with cGAS and sufficient to provide saturated binding. As a result, the enhanced substrate binding does not correlate with cGAS activity (Figs 3J and K, and 4F and G).

Besides DNA, Mn^{2+} alone is able to activate cGAS in the absence of DNA and LLPS. Mn^{2+}-activated cGAS adopts a similar conformation as the DNA-activated one (52, 54). Unlike DNA-induced cGAS activation, our results revealed that truncation of N-terminus and mutations in site B, site C and dimer interface do not abolish Mn^{2+}-induced activation (Figure S10C, Supplementary Material), which emphasizes their mechanistic difference. K384E mutation, located in the site A, completely abolished Mn^{2+}-induced activation, suggesting this site might directly involve in structural rearrangement or enzymatic process of the catalytic center (Figure S10C, Supplementary Material).

Controversy has been raised in the literatures regarding how to differentiate aggregates of molecules and phase-separation-induced condensates (69–71). The interactions of cGAS and DNA are mainly driven by electrostatic forces among protein domains and DNA helixes, which are visualized in published structures (29, 49, 51). Based on our measurements, the concentration of cGAS with micronscale condensates is ~16 μM (Fig. 2E), indicating the cGAS–DNA condensates are not densely packed. In addition, cGAS exhibits similar activity, quantified as cGAMP production per cGAS molecule, in nanoscale and micronscale condensates (Figure S8C, Supplementary Material). Thus, we speculated that, when above the critical concentration, formation of cGAS–DNA condensates, regardless of their sizes, is driven by LLPS. When below the critical concentration, the majority of cGAS and DNA molecules remain in the diluted phase without interacting with each other, whereas a minor proportion of them form small cGAS–DNA heterocomplexes (< 60 nm). Quantifying local concentration within the condensed phase and size-dependent activity might provide hints to

differentiate aggregates and phase-separation-induced condensates.

LLPS has been proposed to utilize several mechanisms to function in cells, including concentrating or excluding molecules of interest, buffering, enhancing interaction between molecules, and accelerating reactions (33). Although LLPS is not the direct factor to activate cGAS, it provides concentrated cGAS and DNA to enhance binding between them at four essential activation sites. Thus, LLPS is essential to activate cGAS *in vivo*. More importantly, the enrichment of the four-sites-bound state and the enhancement of activity of cGAS can be up to the fourth power of the enrichment in concentrations until the four-sites-bound state becomes dominant, which is the fundamental mechanism to explain how phase separation promotes cGAS activity in a none-to-all fashion. Similar mechanisms might be generally used by LLPS to construct on/off switches to achieve switchlike responses in regulating downstream process, such as in transcription regulation (72). Together, our studies not only shed lights on the molecular mechanism of phase-separation-mediated cGAS activation, but also provide guidance and quantitative tools to elucidate mechanisms of LLPS of other biomolecules.

Materials and Methods

Phase separation detected by dcFCCS

According to our previous procedure (42), dcFCCS measurements were performed on a home-built confocal microscope, based on a Zeiss AXIO Observer D1 fluorescence microscope with an oil-immersion objective (100x, NA = 1.4), solid-state 488 and 640 nm excitation lasers (Coherent Inc. OBIS Smart Lasers) and avalanche photodiode (APD) detectors (Excelitas, SPCM-AQRH-14). Fluorescence excited passed through a 50-μm diameter pinhole and was split by a T635lpxr dichroic mirror (Chroma). Fluorescence was further filtered by bandpass filters ET525/50 m for AF488 detection channel (Chroma) and ET700/75 m for Cy5 detection channel (Chroma), and detected by APDs. It took 2 min to mix the samples well, load them onto slides, turn on the lasers and detectors, and initiate data collection. Raw data of photon arriving time was recorded for another 5 min. At least three repeats were performed for each experiment.

In most conditions, dcFCCS experiments were performed with 488 and 640 nm lasers at 25°C in 20 mM Tris-HCl pH 7.5, 100 mM NaCl, 5 mM $MgCl_2$. To examine the effects of Mn^{2+} and Zn^{2+} on phase separation, 5 mM $MnCl_2$ or 200 μM $ZnCl_2$ were added in 20 mM Tris-HCl pH 7.5, 100 mM NaCl, separately. The specific types and concentrations of protein and DNA are indicated in each figure legend and the corresponding schematics.

Analysis of dcFCCS data

Autocorrelation and cross-correlation curves were calculated using collected raw photon arriving time by a home-made MATLAB script. Autocorrelation curves of AF488 and Cy5 detection channels were fitted using Eq. 1.

$$G(\tau) = A\frac{1}{\left(1+\frac{\tau}{\tau_D}\right)}\frac{1}{\sqrt{\left(1+\frac{\tau}{a^2\tau_D}\right)}}\left(1+\frac{T}{1-T}\cdot e^{-\frac{\tau}{\tau_{tri}}}\right), \quad (1)$$

in which A is the amplitude of the autocorrelation curve, τ_D is the diffusion time of the labeled molecules, T is the triplet-state fraction, τ_{tri} is the relaxation time of the triplet state, and a is the ratio of the vertical radius of the laser over its horizontal radius. Herein, A_{488} and A_{640} were calculated as the amplitudes of the autocorrelation curves of AF488 and Cy5 detection channels, respectively.

The cross-correlation curves were fitted using Eq. 2.

$$G_x(\tau) = A_x\frac{1}{\left(1+\frac{\tau}{\tau_{Dx}}\right)}\frac{1}{\sqrt{\left(1+\frac{\tau}{a^2\tau_{Dx}}\right)}}, \quad (2)$$

in which A_x is the amplitude of the cross-correlation curve, τ_{Dx} is the diffusion time of the dual-labeled molecules.

When there are multicomponents in the solution, the amplitudes of the autocorrelation curves (A_{488} and A_{640}) and cross-correlation curves (A_x) can be expressed as

$$A_{488} = \frac{1}{N_A V_{488}}\frac{\sum_i \eta_{488,i}^2 c_i}{\left[\sum_i \eta_{488,i} c_i\right]^2}, \quad (3)$$

$$A_{640} = \frac{1}{N_A V_{640}}\frac{\sum_i \eta_{640,i}^2 c_i}{\left[\sum_i \eta_{640,i} c_i\right]^2}, \quad (4)$$

$$A_x = \frac{1}{N_A V_x}\frac{\sum_i \eta_{488,i}\eta_{640,i}\, c_i}{\left[\sum_i \eta_{488,i} c_i\right]\left[\sum_i \eta_{640,i} c_i\right]}, \quad (5)$$

where $\eta_{488,\,i}$ and $\eta_{640,\,i}$ are the brightness of the species i in the AF488 and Cy5 detection channels, respectively. c_i is the concentration of the species i. N_A is the Avogadro constant. V_{488}, V_{640}, and V_x represent the effective detection volumes of the AF488, Cy5, and cross-correlation detection channels, respectively.

When interactions of AF488-labeled molecules and Cy5-labeled molecules do not lead to formation of condensates or oligomerization, the brightness ($\eta_{488,\,i}$ and $\eta_{640,\,i}$) can be ignored in Eqs. 3–5. Then, the fraction of AF488-labeled molecules forming dual-labeled molecules can be calculated by

$$\frac{N_x}{N_{488}} = \frac{A_x}{A_{640}\times\left(V_{640}/V_x\right)}, \quad (6)$$

and the fraction of Cy5-labeled molecules forming dual-labeled molecules can be calculated by

$$\frac{N_x}{N_{640}} = \frac{A_x}{A_{488}\times\left(V_{488}/V_x\right)}. \quad (7)$$

According to previous procedure, correction factor V_{488}/V_x and V_{640}/V_x of our instrument were determined to be 0.6 and 0.66, respectively, which were based on a dual-labeled dsDNA containing both AF488 and Cy5 (73, 74). However, nanoscale condensates should contain species of different size and brightness, whose size might follow a narrow distribution (42). Thus, under these conditions, the corrected A_x/A_{640} and A_x/A_{488} should only be used as semiquantitative values to provide a rough estimation of proportions of AF488-cGAS and Cy5-DNA participating in condensates, respectively.

Fluorophore AF488, whose diffusion time and radius were 0.09 ms and 0.58 nm, respectively, was used as a standard sample to calibrate the instrument and to calculate hydrodynamic radii of condensates via Stokes–Einstein equation (75).

Quantifying binding affinities of DNA with cGAS via dcFCCS

To quantify binding affinities between DNA and cGAS, dcFCCS experiments were performed with AF488-labeled cGAS and Cy5-labeled DNA in 20 mM Tris-HCl pH 7.5, 100 mM NaCl, and 5 mM

$MgCl_2$ at 25°C. For 15 and 20 bp DNAs, 50 nM cGAS and 100 nM DNA were used. For 25 bp DNA, 10 nM cGAS and 20 nM DNA were used. Fractions of Cy5-labeled DNA forming dual-labeled cGAS–DNA complex were calculated by Eq. 7, with which binding constant of cGAS and DNA can be calculated. Other cGAS variants with 25 bp DNA followed the same procedure. Raw data of photon arriving time and FCS curves were recorded for 5 min right after mixing samples. At least three repeats of dcFCCS measurements were performed for each condition.

Burst analysis and estimation of stoichiometry

Briefly, raw data of photon were binned into 1-ms bins to generate fluorescence trajectories. Only bursts exceeding the threshold, defined as three SDs above the mean, were selected to calculate intensity ratio of AF488 and Cy5 detection channel (I_{AF488}/I_{Cy5}) by a home-made MATLAB script. The individual brightness of labeled molecules was estimated by the product of fluorescence intensity and amplitude of autocorrelation curve in the corresponding detection channels. After calibration, the stoichiometry was calculated from I_{AF488}/I_{Cy5} using the molecular brightness of Alexa Fluor 488 and Cy5 (η_{488} and η_{640}), and correcting FRET between AF488 and Cy5 within condensates. The FRET efficiencies were quantified by fluorescence lifetime of AF488, measured by a commercial FV1200 confocal fluorescence lifetime microscope (Figure S4B–D, Supplementary Material).

See Supplementary Material Appendix for further details of sample preparation, spinning disk confocal microscopy, quantifying binding affinity of cGAS dimer, and binding affinities of ATP and GTP with cGAS, TIRF microscopy, and cGAS activity assay.

Acknowledgments

The authors would like to acknowledge the Cell Imaging Facility, Tsinghua University for the assistance.

Supplementary Material

Supplementary material is available at *PNAS Nexus* online.

Funding

This project was supported by grants from the National Natural Science Foundation of China (21922704, 21877069, and 22061160466 to C.C. and 22007054 to W.W.), Tsinghua-Peking Joint Center for Life Sciences, Beijing Advanced Innovation Center for Structural Biology. and Beijing Frontier Research Center for Biological Structure to C.C.

Authors' Contributions

YY and CC designed research, YY performed research, YY, WW and CC contributed new reagents or analytic tools, YY and CC analyzed data and wrote the paper.

Data Availability

All data are available in the manuscript and Supplementary Material Appendix.

References

1. Gallucci S, Maffei ME. 2017. DNA sensing across the Tree of Life. Trends Immunol. 38(10):719–732.
2. Seong SY, Matzinger P. 2004. Hydrophobicity: an ancient damage-associated molecular pattern that initiates innate immune responses. Nat Rev Immunol. 4(6):469–478.
3. Medzhitov R, Janeway C, Jr. 2000. Innate immune recognition: mechanisms and pathways. Immunol Rev. 173:89–97.
4. Hemmi H, *et al.* 2000. A Toll-like receptor recognizes bacterial DNA. Nature. 408(6813):740–745.
5. Hornung V, *et al.* 2009. AIM2 recognizes cytosolic dsDNA and forms a caspase-1-activating inflammasome with ASC. Nature. 458(7237):514–518.
6. Wu J, *et al.* 2013. Cyclic GMP-AMP is an endogenous second messenger in innate immune signaling by cytosolic DNA. Science. 339(6121):826–830.
7. Ablasser A, *et al.* 2013. cGAS produces a 2′-5′-linked cyclic dinucleotide second messenger that activates STING. Nature. 498(7454):380–384.
8. Diner EJ, *et al.* 2013. The innate immune DNA sensor cGAS produces a noncanonical cyclic dinucleotide that activates human STING. Cell Rep. 3(5):1355–1361.
9. Zhang X, *et al.* 2013. Cyclic GMP-AMP containing mixed phosphodiester linkages is an endogenous high-affinity ligand for STING. Mol Cell. 51(2):226–235.
10. Sun L, Wu J, Du F, Chen X, Chen ZJ. 2013. Cyclic GMP-AMP synthase is a cytosolic DNA sensor that activates the type I interferon pathway. Science. 339(6121):786–791.
11. Cai X, Chiu YH, Chen ZJ. 2014. The cGAS-cGAMP-STING pathway of cytosolic DNA sensing and signaling. Mol Cell. 54(2):289–296.
12. Lam E, Stein S, Falck-Pedersen E. 2014. Adenovirus detection by the cGAS/STING/TBK1 DNA sensing cascade. J Virol. 88(2): 974–981.
13. Gao D, *et al.* 2013. Cyclic GMP-AMP synthase is an innate immune sensor of HIV and other retroviruses. Science. 341(6148):903–906.
14. Majlessi L, Brosch R. 2015. *Mycobacterium tuberculosis* meets the cytosol: the role of cGAS in anti-mycobacterial immunity. Cell Host Microbe. 17(6):733–735.
15. Watson RO, *et al.* 2015. The cytosolic sensor cGAS detects *Mycobacterium tuberculosis* DNA to induce type I interferons and activate autophagy. Cell Host Microbe. 17(6):811–819.
16. Collins AC, *et al.* 2015. Cyclic GMP-AMP synthase is an innate immune DNA sensor for *Mycobacterium tuberculosis*. Cell Host Microbe. 17(6):820–828.
17. Neufeldt CJ, *et al.* 2020. SARS-CoV-2 infection induces a pro-inflammatory cytokine response through cGAS-STING and NF-κB. Commun Biol. 5:45. DOI: 10.1101/2020.1107.1121.212639.
18. Rui Y, *et al.* 2021. Unique and complementary suppression of cGAS-STING and RNA sensing- triggered innate immune responses by SARS-CoV-2 proteins. Signal Transduct Target Ther. 6(1):123.
19. Han L, *et al.* 2021. SARS-CoV-2 ORF9b antagonizes type I and III interferons by targeting multiple components of the RIG-I/MDA-5-MAVS, TLR3-TRIF, and cGAS-STING signaling pathways. J Med Virol. 93(9):5376–5389.
20. Zierhut C, Funabiki H. 2020. Regulation and consequences of cGAS activation by self-DNA. Trends Cell Biol. 30(8):594–605.
21. Deng L, *et al.* 2014. STING-dependent cytosolic DNA sensing promotes radiation-induced type I interferon-dependent antitumor immunity in immunogenic tumors. Immunity. 41(5):843–852.
22. Woo SR, *et al.* 2014. STING-dependent cytosolic DNA sensing mediates innate immune recognition of immunogenic tumors. Immunity. 41(5):830–842.
23. Civril F, *et al.* 2013. Structural mechanism of cytosolic DNA sensing by cGAS. Nature. 498(7454):332–337.

24. Kranzusch PJ, Lee AS, Berger JM, Doudna JA. 2013. Structure of human cGAS reveals a conserved family of second-messenger enzymes in innate immunity. Cell Rep. 3(5):1362–1368.
25. Kranzusch PJ, Vance RE. 2013. cGAS dimerization entangles DNA recognition. Immunity. 39(6):992–994.
26. Zhang X, *et al.* 2014. The cytosolic DNA sensor cGAS forms an oligomeric complex with DNA and undergoes switch-like conformational changes in the activation loop. Cell Rep. 6(3): 421–430.
27. Gao P, *et al.* 2013. Cyclic [G(2′,5′)pA(3′,5′)p] is the metazoan second messenger produced by DNA-activated cyclic GMP-AMP synthase. Cell. 153(5):1094–1107.
28. Andreeva L, *et al.* 2017. cGAS senses long and HMGB/TFAM-bound U-turn DNA by forming protein-DNA ladders. Nature. 549(7672):394–398.
29. Li X, *et al.* 2013. Cyclic GMP-AMP synthase is activated by double-stranded DNA-induced oligomerization. Immunity. 39(6): 1019–1031.
30. Du M, Chen ZJ. 2018. DNA-induced liquid phase condensation of cGAS activates innate immune signaling. Science. 361(6403):704–709.
31. Xu G, *et al.* 2021. Viral tegument proteins restrict cGAS-DNA phase separation to mediate immune evasion. Mol Cell. 81: 1–15.
32. Hyman AA, Weber CA, Julicher F. 2014. Liquid-liquid phase separation in biology. Annu Rev Cell Dev Biol. 30:39–58.
33. Banani SF, Lee HO, Hyman AA, Rosen MK. 2017. Biomolecular condensates: organizers of cellular biochemistry. Nat Rev Mol Cell Biol. 18(5):285–298.
34. Sheu-Gruttadauria J, MacRae IJ. 2018. Phase transitions in the assembly and function of human miRISC. Cell. 173(4):946–957.e916.
35. Xia S, Chen Z, Shen C, Fu TM. 2021. Higher-order assemblies in immune signaling: supramolecular complexes and phase separation. Protein Cell. 12(9):680–694.
36. David L, *et al.* 2018. Assembly mechanism of the CARMA1-BCL10-MALT1-TRAF6 signalosome. Proc Natl Acad Sci USA. 115(7):1499–1504.
37. Su X, *et al.* 2016. Phase separation of signaling molecules promotes T cell receptor signal transduction. Science. 352(6285):595–599.
38. Tao J, *et al.* 2017. Nonspecific DNA binding of cGAS N terminus promotes cGAS activation. J Immunol. 198(9):3627–3636.
39. Luecke S, *et al.* 2017. cGAS is activated by DNA in a length-dependent manner. EMBO Rep. 18(10):1707–1715.
40. Hu MM, Shu HB. 2020. Innate immune response to cytoplasmic DNA: mechanisms and diseases. Annu Rev Immunol. 38:79–98.
41. Zhou W, Mohr L, Maciejowski J, Kranzusch PJ. 2021. cGAS phase separation inhibits TREX1-mediated DNA degradation and enhances cytosolic DNA sensing. Mol Cell. 81(4):739–755.e737.
42. Peng S, *et al.* 2020. Phase separation at the nanoscale quantified by dcFCCS. Proc Natl Acad Sci USA. 117(44):27124–27131.
43. Stetefeld J, McKenna SA, Patel TR. 2016. Dynamic light scattering: a practical guide and applications in biomedical sciences. Biophys Rev. 8(4):409–427.
44. Hooy RM, Sohn J. 2018. The allosteric activation of cGAS underpins its dynamic signaling landscape. Elife. 7:e39984.
45. Stetson DB, Medzhitov R. 2006. Recognition of cytosolic DNA activates an IRF3-dependent innate immune response. Immunity. 24(1):93–103.
46. Kato K, Omura H, Ishitani R, Nureki O. 2017. Cyclic GMP-AMP as an endogenous second messenger in innate immune signaling by cytosolic DNA. Annu Rev Biochem. 86:541–566.
47. Lee A, Park EB, Lee J, Choi BS, Kang SJ. 2017. The N terminus of cGAS de-oligomerizes the cGAS:DNA complex and lifts the DNA size restriction of core-cGAS activity. FEBS Lett. 591(6): 954–961.
48. Gentili M, *et al.* 2019. The N-terminal domain of cGAS determines preferential association with centromeric DNA and innate immune activation in the nucleus. Cell Rep. 26(9): 2377–2393.e2313.
49. Xie W, *et al.* 2019. Human cGAS catalytic domain has an additional DNA-binding interface that enhances enzymatic activity and liquid-phase condensation. Proc Natl Acad Sci USA. 116(24):11946–11955.
50. Decout A, Ablasser A. 2018. Human cGAS has a slightly different taste for dsDNA. Immunity. 49(2):206–208.
51. Zhou W, *et al.* 2018. Structure of the human cGAS-DNA complex reveals enhanced control of immune surveillance. Cell. 174(2):300–311.e311.
52. Zhao Z, *et al.* 2020. Mn(2+) directly activates cGAS and structural analysis suggests Mn(2+) induces a noncanonical catalytic synthesis of 2′3′-cGAMP. Cell Rep. 32(7):108053.
53. Wang C, *et al.* 2018. Manganese increases the sensitivity of the cGAS-STING pathway for double-stranded DNA and is required for the host defense against DNA viruses. Immunity. 48(4):675–687.e677.
54. Hooy RM, Massaccesi G, Rousseau KE, Chattergoon MA, Sohn J. 2020. Allosteric coupling between Mn2+ and dsDNA controls the catalytic efficiency and fidelity of cGAS. Nucleic Acids Res. 48(8):4435–4447.
55. Fabrini R, *et al.* 2009. Monomer-dimer equilibrium in glutathione transferases: a critical re-examination. Biochemistry. 48(43):10473–10482.
56. Ablasser A, Chen ZJ. 2019. cGAS in action: expanding roles in immunity and inflammation. Science. 363(6431): eaat8657.
57. Zhao Q, Wei Y, Pandol SJ, Li L, Habtezion A. 2018. STING signaling promotes inflammation in experimental acute pancreatitis. Gastroenterology. 154(6):1822–1835.e1822.
58. Kerur N, *et al.* 2018. cGAS drives noncanonical-inflammasome activation in age-related macular degeneration. Nat Med. 24(1):50–61.
59. Song ZM, *et al.* 2020. KAT5 acetylates cGAS to promote innate immune response to DNA virus. Proc Natl Acad Sci USA. 117(35):21568–21575.
60. Lian H, *et al.* 2018. ZCCHC3 is a co-sensor of cGAS for dsDNA recognition in innate immune response. Nat Commun. 9(1): 3349.
61. Liu ZS, *et al.* 2019. G3BP1 promotes DNA binding and activation of cGAS. Nat Immunol. 20(1):18–28.
62. Huang J, *et al.* 2018. Herpes Simplex Virus 1 tegument protein VP22 abrogates cGAS/STING-mediated antiviral innate immunity. J Virol. 92(15):e00841–e00818.
63. Wu JJ, *et al.* 2015. Inhibition of cGAS DNA sensing by a herpesvirus virion protein. Cell Host Microbe. 18(3):333–344.
64. Zhang X, Bai XC, Chen ZJ. 2020. Structures and mechanisms in the cGAS-STING innate immunity pathway. Immunity. 53(1): 43–53.
65. Chen S, Rong M, Lv Y, Zhu D, Xiang Y. 2020. Regulation of cGAS activity through RNA-mediated phase separation. bioRxiv. DOI: 10.1101/2020.1109.1127.316166.
66. Kuznetsova IM, Zaslavsky BY, Breydo L, Turoverov KK, Uversky VN. 2015. Beyond the excluded volume effects: mechanistic complexity of the crowded milieu. Molecules. 20(1): 1377–1409.

67. Ralston GB. 1990. Effects of "crowding" in protein solutions. J Chem Educ. 67(10):857.
68. Traut TW. 1994. Physiological concentrations of purines and pyrimidines. Mol Cell Biochem. 140(1):1–22.
69. Musacchio A. 2022. On the role of phase separation in the biogenesis of membraneless compartments. EMBO J. 41(5):e109952.
70. Rana U, Brangwynne CP, Panagiotopoulos AZ. 2021. Phase separation vs aggregation behavior for model disordered proteins. J Chem Phys. 155(12):125101.
71. Zhou HX, Nguemaha V, Mazarakos K, Qin S. 2018. Why do disordered and structured proteins behave differently in phase separation?. Trends Biochem Sci. 43(7):499–516.
72. Sabari BR, *et al.* 2018. Coactivator condensation at superenhancers links phase separation and gene control. Science. 361(6400):eaar3958.
73. Werner S, Ebenhan J, Haupt C, Bacia K. 2018. A quantitative and reliable calibration standard for dual-color fluorescence cross-correlation spectroscopy. ChemPhysChem. 19(24):3436–3444.
74. Bacia K, Haustein E, Schwille P. 2014. Fluorescence correlation spectroscopy: principles and applications. Cold Spring Harb Protoc. 2014(7):709–725.
75. Heyman NS, Burt JM. 2008. Hindered diffusion through an aqueous pore describes invariant dye selectivity of Cx43 junctions. Biophys J. 94(3):840–854.